Raman spectroscopy study of the phase transitions in $Pb_{0.99}Nb_{0.02}[(Zr_{0.57}Sn_{0.43})_{1-y}Ti_y]_{0.98}O_3$ ceramics

2007 J. Phys.: Condens. Matter 19 136003

(http://iopscience.iop.org/0953-8984/19/13/136003)

IOP PUBLISHING JOURNAL OF PHYSICS: CONDENSED MATTER

J. Phys.: Condens. Matter **19** (2007) 136003 (13pp) doi:10.1088/0953-8984/19/13/136003

Raman spectroscopy study of the phase transitions in $Pb_{0.99}Nb_{0.02}[(Zr_{0.57}Sn_{0.43})_{1-y}Ti_y]_{0.98}O_3$ ceramics

H He and X Tan[1]

Department of Materials Science and Engineering, Iowa State University, Ames, IA 50011, USA

E-mail: xtan@iastate.edu

Received 25 October 2006, in final form 1 February 2007
Published 12 March 2007
Online at stacks.iop.org/JPhysCM/19/136003

Abstract

Detailed studies of the phase transitions in $Pb_{0.99}Nb_{0.02}[(Zr_{0.57}Sn_{0.43})_{1-y}Ti_y]_{0.98}O_3$ ($y = 0.03$, 0.04, 0.05, 0.06, 0.07, 0.08, 0.10, and 0.12) ceramics as a function of composition, temperature, electric field, and time were conducted using Raman spectroscopy. At room temperature, the as-sintered ceramics with $y = 0.03$–0.08 show an antiferroelectric order while those with $y = 0.10$ and 0.12 show a ferroelectric order. For the ceramic with $y = 0.08$, however, a ferroelectric order can also be stabilized at room temperature when it is warmed up from lower temperatures. The electric field-induced ferroelectric phase in the ceramic with $y = 0.07$ is metastable at room temperature and ages back to the stable antiferroelectric phase on a timescale of hours.

1. Introduction

The $PbZrO_3$-based antiferroelectric ceramics are of technological importance due to their wide applications in microelectromechanical systems and energy storage devices [1–3]. The electric field-induced antiferroelectric-to-ferroelectric phase transition forms the physics basis for these applications. The most intensively studied antiferroelectric materials are chemically modified $PbZrO_3$ by adding Sn, Ti, and Nb or La to adjust the critical field for the phase transition and to optimize the properties for processing and applications [1–7]. It has been widely accepted that the optimized properties in these ceramics are resulted from their hierarchical microstructures: the subgrain level antiferroelectric 90° domains (the checkerboard pattern) and the nanoscale incommensurate modulations within the domains [6–13]. Increase in Ti content eventually destroys these microstructures and leads to a normal ferroelectric behaviour.

Raman spectroscopy has been extensively used in the study of the phase transition in ferroelectric oxides [14–17]. The subtle changes in bond distance, bond angle and crystal symmetry during phase transitions can be revealed by the change in the mode frequency and the presence/absence of different modes. In most $PbZrO_3$-based ceramics, the presence of many

[1] Author to whom any correspondence should be addressed.

modes at low frequencies (less than 150 cm^{-1}) is the characteristics of the antiferroelectric order [18–26]. These intense low frequency modes were assigned to the bonds between the Pb cation and other ions in the unit cell [18]. Although the normal Raman modes can be predicted from crystal symmetry, the actual frequency and intensity of each mode are strongly dependent on chemical composition and processing conditions. El-Harrad *et al* [21] studied the phase transitions in $Pb(Zr_{0.95}Ti_{0.05})O_3$ ceramics with Raman spectroscopy and found that 1 wt% doping of La_2O_3 does not lead to any change in the spectra but 1 wt% Nb_2O_5 doping changes the Raman spectra significantly. Several phases, including the incommensurate antiferroelectric one, have been observed in Sn-modified antiferroelectric $Pb(Zr, Ti)O_3$ ceramics [1–7]. However, to the authors' knowledge, Raman spectroscopy study on these antiferroelectric ceramics with incommensurate modulations has not yet been reported. In the present work, experimental studies with Raman spectroscopy on the composition-, temperature-, electric field-, and time-induced phase transitions in the $Pb_{0.99}Nb_{0.02}[(Zr_{0.57}Sn_{0.43})_{1-y}Ti_y]_{0.98}O_3$ series were conducted.

2. Experimental procedure

$Pb_{0.99}Nb_{0.02}[(Zr_{0.57}Sn_{0.43})_{1-y}Ti_y]_{0.98}O_3$ (abbreviated as PNZST $43/100y/2$) solid solutions with $y = 0.03$, 0.04, 0.05, 0.06, 0.07, 0.08, 0.10, and 0.12 were prepared by the conventional solid state reaction method from high purity oxides. Raw powders with purity better than 99.9% of PbO, Nb_2O_5, ZrO_2, SnO_2, and TiO_2 were batched according to the chemical formula with 5% excess PbO powder to compensate for the lead evaporation loss in the subsequent thermal process. The powders were calcined at 850 °C for 4 h in a covered alumina crucible for two times to ensure the chemical homogeneity and the phase purity. Sintering was performed at 1300 °C for 3 h using $PbZrO_3$ as protective powder.

After removal of surface layers by mechanical grinding, these ceramics were checked by x-ray diffraction for phase purity and scanning electron microscopy (SEM) for grain morphology. Dielectric characterization was conducted with an LCR meter (HP-4284A, Hewlett-Packard) at frequency of 1 kHz in conjunction with an environmental chamber. A heating/cooling rate of 3 °C min^{-1} was used during measurement. Electric field-induced polarization was recorded with a standardized ferroelectric test system (RT-66A, Radiant technologies).

For the Raman spectroscopy experiments, one specimen for each composition was polished and subsequently annealed at 200 °C for 30 min to relieve the residual stress caused by cutting and polishing. A set of Raman scattering spectra were collected at room temperature with a Renishaw inVia spectrometer using the 488 nm line of the Ar^+ laser at 50 mW of power. The instrument was calibrated using an internal silicon reference, and the bands were reproducible within ± 1 cm^{-1}. The laser beam was focused with a 50× lens, producing a beam size of 3–5 μm on the polished specimen surface. Raman scattering experiment was also performed under controlled temperature in the range of −50 to 250 °C. A heating/cooling rate of 3 °C min^{-1} was used during the test. The temperature was kept for 10 min at each predetermined point prior to recording the Raman spectrum. The Raman data were collected from exactly the same grain at different temperatures.

For the PNZST 43/7/2 specimen, two additional Raman experiments were conducted at room temperature: one *in situ* experiment and one ageing test. The *in situ* experiment was designed to monitor the electric field-induced antiferroelectric-to-ferroelectric phase transition. Two gold electrodes with spacing of 1 mm were sputter deposited on one polished surface and copper wires were soldered to the Au electrodes using silver conductive epoxy. The high voltage side of the Au electrodes was covered by insulation varnish to prevent arcing. High static electric fields were applied to the sample with a high voltage power supply

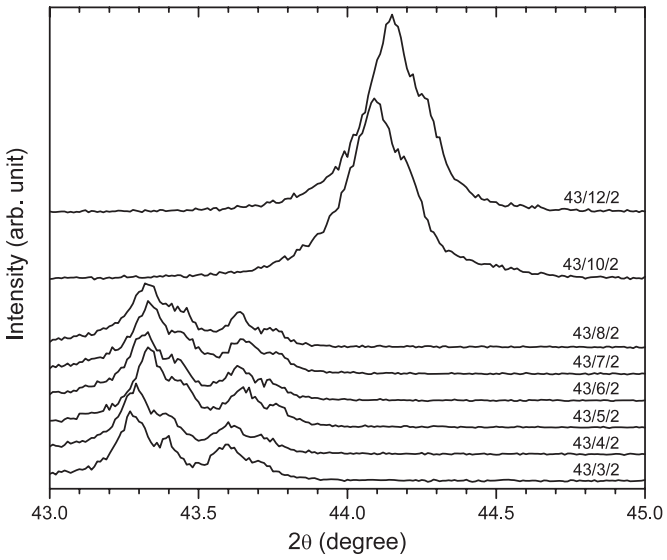

Figure 1. X-ray diffraction spectra for the as-sintered $Pb_{0.99}Nb_{0.02}[(Zr_{0.57}Sn_{0.43})_{1-y}Ti_y]_{0.98}O_3$ ceramics.

(Model 610D, Trek). Acquisition of Raman spectra was completed at a series of field strengths. The ageing experiment was intended to reveal the backward ferroelectric-to-antiferroelectric phase transition from the metastable induced ferroelectric phase. For this experiment, a disc sample was electroded with carbon paste on both faces and poled under an electric field of 20 kV cm^{-1} along the thickness direction. The carbon paste electrodes were then dissolved with acetone and Raman spectra were collected from the same grain as a function of time.

3. Results and discussion

3.1. Structure and electrical properties

X-ray diffraction shows that all the as-sintered ceramics are phase pure with the perovskite structure. Full spectrum analysis indicates that the ceramics with $y = 0.03$–0.08 display an orthorhombic while those with $y = 0.10$ and 0.12 exhibit a rhombohedral symmetry. This can be clearly seen from the partial spectrum for the pseudocubic 200 peak with 2θ in the range of 43.0°–45° shown in figure 1. However, it should be noted that there might be a second phase present in the surface layer of the ceramics, with the content level below the x-ray detection limit, especially for compositions PNZST 43/8/2 and PNZST 43/10/2. From previous studies on ceramics with similar compositions [1–7], the orthorhombic phase is expected to be antiferroelectric while the rhombohedral phase is ferroelectric. However, the orthorhombic symmetry has been mistakenly believed to be tetragonal symmetry previously [1, 2]. As Viehland pointed out, a tetragonal structure does not support the antiferroelectric order [6]. Furthermore, our synchrotron x-ray diffraction experiment has determined the space group as $Bmm2$ [27]. Previous studies suggest the space group $R3c$ for the rhombohedral phase for compositions $y = 0.10$ and 0.12 at room temperature [4–7].

Density and grain size of the ceramic was examined in three representative compositions, namely PNZST 43/3/2, PNZST 43/6/2 and PNZST 43/12/2. It is found that high relative density (94%, 96%, and 94% for PNZST 43/3/2, 43/6/2, and 43/12/2, respectively) was

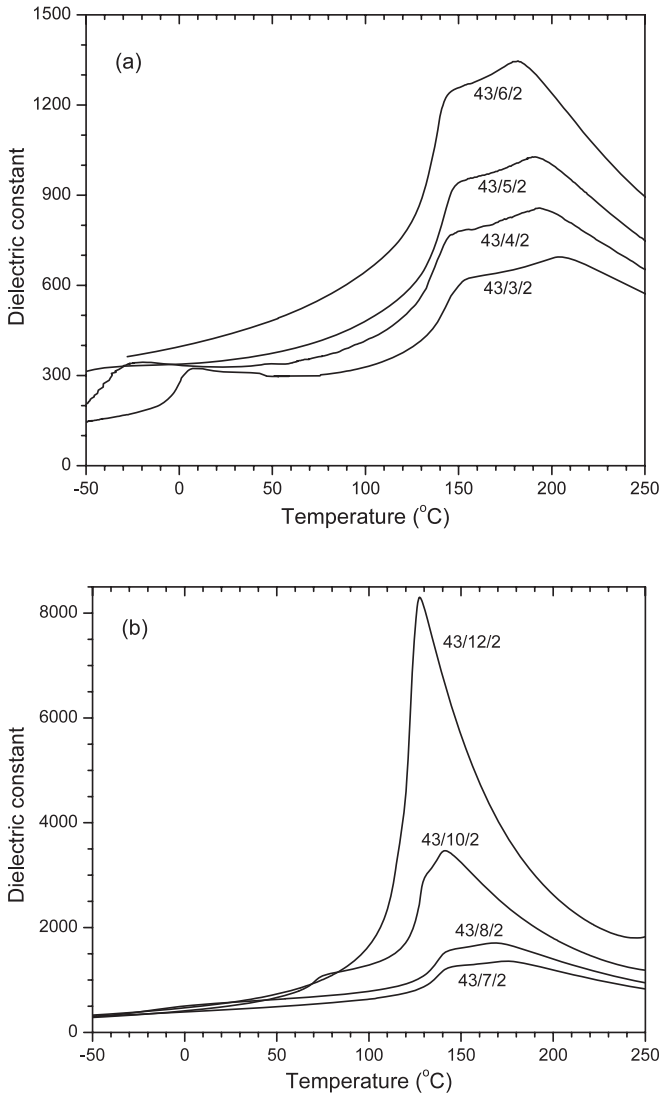

Figure 2. Dielectric constant of the $Pb_{0.99}Nb_{0.02}[(Zr_{0.57}Sn_{0.43})_{1-y}Ti_y]_{0.98}O_3$ ceramics measured at 1 kHz during cooling.

achieved in these ceramics. Grain morphologies were analysed with SEM and the grain size was determined from the SEM micrographs to be 4.2, 3.2, and 4.3 μm for PNZST 43/3/2, 43/6/2, and 43/12/2, respectively. The grain size is essentially the same as the size of the laser beam used in the Raman spectroscopy experiments.

The dielectric constant as a function of temperature was measured for these ceramics at 1 kHz. Figure 2 shows the results obtained from cooling at a rate of 3 °C min^{-1}. Different scales along the ordinate were used in figures 2(a) and (b) for clarity. It is evident that as Ti content increases, the maximum dielectric constant increases dramatically. From previous studies on ceramics with similar compositions, PNZST 43/3/2, PNZST 43/4/2, and PNZST 43/5/2 show two antiferroelectric phases in the measuring temperature range. For PNZST 43/3/2,

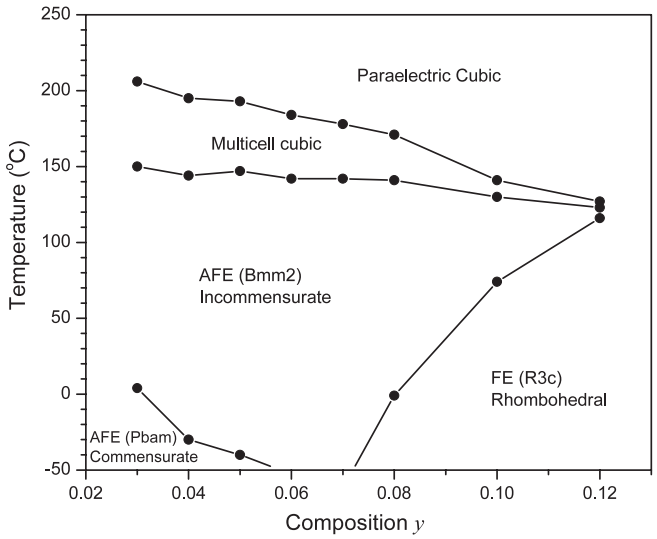

Figure 3. The temperature versus composition phase diagram for the $Pb_{0.99}Nb_{0.02}[(Zr_{0.57}Sn_{0.43})_{1-y}Ti_y]_{0.98}O_3$ ceramics derived from figure 2.

the transition temperature between the two antiferroelectric phases is at 4 °C, while that for PNZST 43/4/2 and PNZST 43/5/2 are at −30 and −40 °C, respectively. The antiferroelectric phase at lower temperatures is commensurate and isostructural to $PbZrO_3$ with the *Pbam* space group [6]. The high temperature antiferroelectric phase has incommensurate modulations with the space group *Bmm*2 [27]. The incommensurate antiferroelectric phase persists to temperatures below −50 °C (the lower limit for our dielectric characterization) as Ti increases to $y = 0.06$ and 0.07. However, further increase in Ti content leads to the development of a ferroelectric order at lower temperatures and at the same time, the temperature range for the incommensurate phase is suppressed. At $y = 0.12$, the ferroelectric phase is stable below 116 °C, the antiferroelectric phase is stable between 116 and 123 °C. Another feature in figure 2 is the presence of a plateau region in the dielectric response. This was assigned as the multicell cubic phase region between the incommensurate orthorhombic antiferroelectric phase and the paraelectric cubic phase [28]. The multicell cubic region was previously attributed to the disruption of the paraelectric–antiferroelectric transformation by Sn modification [28].

The phase changes discussed above are summarized in a phase diagram, as shown in figure 3. It should be noted that this diagram is based on dielectric constant measurements during cooling. Since all these phase transitions are first order in nature, a slight shift of the phase boundary lines toward higher temperatures is expected if the diagram is constructed on the basis of heating measurement. It shows clearly that the Curie temperature decreases continuously with increasing Ti content. In contrast, the lower temperature limit for the multicell cubic phase is only a weak function of Ti content. The incommensurate antiferroelectric phase spans the widest temperature range at intermediate Ti content of $y = 0.06$ and 0.07. This observation supports the argument that the incommensurate modulation is resulted from the frustration of competing interactions between antiferroelectric and ferroelectric orders [7]. At low temperatures, the antiferroelectric phase (isostructural to $PbZrO_3$) transforms to the ferroelectric phase (isostructural to the R_{LT} phase in lead zirconate titanate) as Ti content increases. At $y = 0.12$, the two intermediate phases, the multicell cubic and the incommensurate antiferroelectric phases, almost disappear. Beyond this composition,

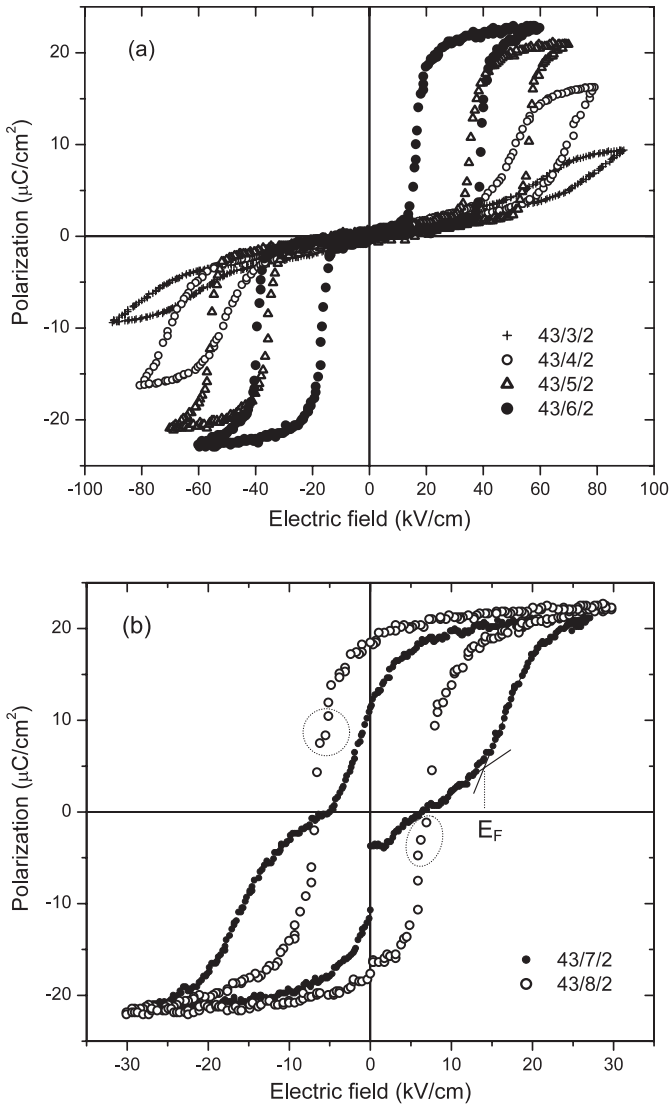

Figure 4. The polarization versus electric field hysteresis loops for the as-sintered $Pb_{0.99}Nb_{0.02}[(Zr_{0.57}Sn_{0.43})_{1-y}Ti_y]_{0.98}O_3$ ceramics. E_F is marked for PNZST 43/7/2 in (b). The slight distortion on the hysteresis loop of PNZST 43/8/2 is indicated by two dotted circles in (b).

the paraelectric cubic phase transforms directly to the ferroelectric rhombohedral phase during cooling.

The antiferroelectric-to-ferroelectric phase transition can also be triggered by applied electric fields. This is revealed by the polarization versus electric field hysteresis loop measurement depicted in figure 4. The measurement was conducted at room temperature with a frequency of 4 Hz. The ceramics with $y = 0.03$, 0.04, 0.05, and 0.06 display the characteristic double hysteresis loops, indicating the occurrence of the electric field-induced antiferroelectric-to-ferroelectric phase transition (figure 4(a)). As Ti content increases, the critical field for the phase transition decreases while the polarization developed in the ferroelectric phase increases.

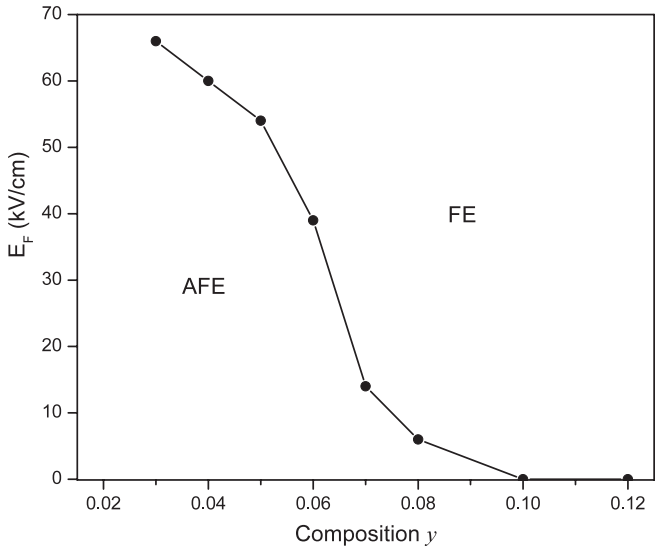

Figure 5. The electric field versus composition phase diagram for the $Pb_{0.99}Nb_{0.02}[(Zr_{0.57}Sn_{0.43})_{1-y}Ti_y]_{0.98}O_3$ ceramics derived from figure 4.

For these four compositions (PNZST 43/3/2, 43/4/2, 43/5/2, and 43/6/2), the induced ferroelectric phase is not stable and the reverse transition takes place during the release of the applied electric fields. For example, the forward antiferroelectric-to-ferroelectric transition occurs at 39 kV cm^{-1} (referred to as E_F in literature) and the reverse transition occurs when the field decreases to 18 kV cm^{-1} (referred to as E_A in literature) in PNZST 43/6/2. Increase further in Ti content to $y = 0.07$ leads to a more sluggish reverse phase transition and a distorted hysteresis loop (figure 4(b)). At the measuring frequency of 4 Hz, a remanent polarization of 10 μC cm^{-2} was observed from figure 4(b), indicating the persistence of the ferroelectric phase at this timescale. As shown in figure 4(b), the E_F is determined to be 14 kV cm^{-1}. PNZST 43/8/2 appears to have a single hysteresis loop as observed in normal ferroelectric ceramics. However, close examination of its hysteresis loop reveals that there is distortion on the loop when the applied field increases for both polarities, as indicated by the two dotted circles in figure 4(b). Therefore, the hysteresis loop of PNZST 43/8/2 bears similarities with PNZST 43/7/2. The E_F is determined to be 6 kV cm^{-1}. Figure 4(b) also reveals a high remanent polarization for PNZST 43/8/2 (18 μC cm^{-2}), indicating a stable ferroelectric phase at room temperature. This will be further discussed in the following section. For compositions of $y = 0.10$ and 0.12, regular single hysteresis loops were observed (not shown). Therefore, the hysteresis loops observed are consistent with both x-ray diffraction and dielectric measurement results. The observations on the electric field-induced phase transition are summarized in an electric field versus composition phase diagram, as shown in figure 5.

3.2. Raman spectroscopy studies

The Raman spectra for all compositions collected at room temperature are presented in figure 6. The modes in low frequency range are focused because most active Raman modes for antiferroelectric $PbZrO_3$ were previously found in this range [18]. Consistent with the results of x-ray diffraction, dielectric and ferroelectric measurement reported in the previous section, the ferroelectric PNZST 43/10/2 and PNZST 43/12/2 ceramics display different

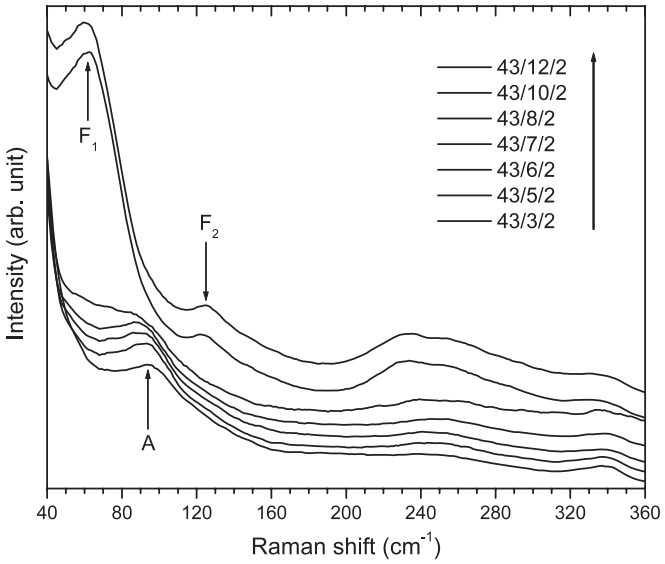

Figure 6. Raman spectra collected at room temperature from the as-sintered $Pb_{0.99}Nb_{0.02}[(Zr_{0.57}Sn_{0.43})_{1-y}Ti_y]_{0.98}O_3$ ceramics.

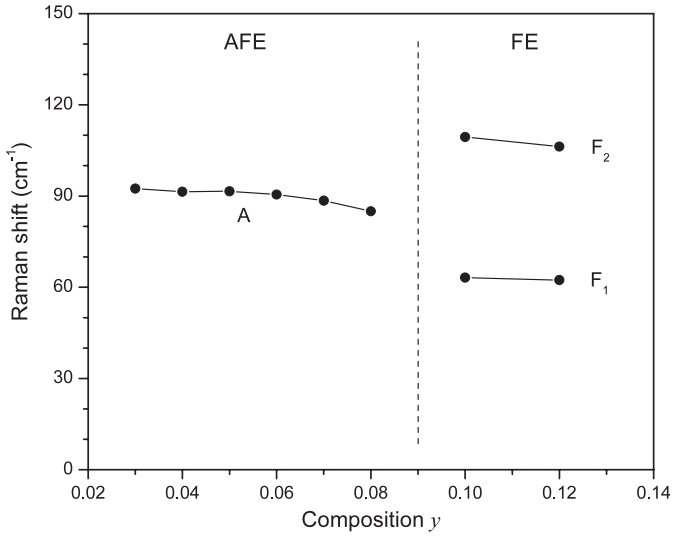

Figure 7. The evolution of the characteristic modes A, F_1, and F_2 as a function of composition y in $Pb_{0.99}Nb_{0.02}[(Zr_{0.57}Sn_{0.43})_{1-y}Ti_y]_{0.98}O_3$ ceramics.

active Raman modes from other ceramics. As Ti content increases from $y = 0.03$ to 0.12, the most prominent feature in the Raman spectra is the softening of the mode around 90 cm^{-1} and the emergence of the modes around 60 and 125 cm^{-1}. The exact frequency of these three modes in different compositions after deconvolution is plotted in figure 7. Since x-ray diffraction, dielectric characterization, and hysteresis loop measurement indicate ferroelectric order in PNZST 43/10/2 and 43/12/2, and antiferroelectric order in others, the mode around 90 cm^{-1} (denoted as mode A hereafter) is the signature of the antiferroelectric phase and the

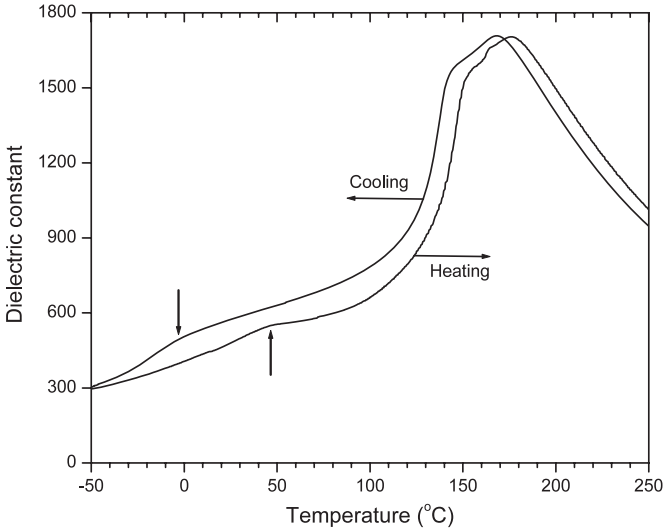

Figure 8. The thermal hysteresis of the antiferroelectric ↔ ferroelectric phase transition (marked by the two vertical arrows) in PNZST 43/8/2 revealed by dielectric constant measurement.

modes around 60 cm^{-1} (denoted as mode F_1 hereafter) and 125 cm^{-1} (denoted as F_2 hereafter) are characteristic of the ferroelectric order. These low frequency modes are believed to be originated from the bonds between the Pb cation and other ions in the unit cell [18] and will be used in the following discussion for identifying different phases.

As discussed in the last section, both antiferroelectric and ferroelectric phases are stable in the PNZST 43/8/2 ceramic at room temperature. This is further confirmed by the dielectric constant measurement during heating from −50 to 250 °C. The result is shown in figure 8, together with that measured during cooling from 250 °C. As marked by the two vertical arrows, the antiferroelectric phase transforms to a ferroelectric phase at around −1 °C during cooling while the ferroelectric phase transforms to an antiferroelectric phase at 45 °C during heating. Therefore, either the ferroelectric or the antiferroelectric phase could be stabilized at room temperature, roughly 25 °C, depending on the thermal history of the ceramic. This is also directly confirmed by Raman spectroscopy study. As shown in figure 9, an obvious antiferroelectric mode A was detected in the sample cooled from 200 °C while strong ferroelectric modes F_1 and F_2 were observed in the sample heated up from −50 °C. Further heating to 75 °C leads to the softening of modes F_1 and F_2 and the emergence of mode A. However, mode A at 75 °C is shifted to a lower frequency than that at 25 °C.

The phase diagram shown in figure 3 indicates that PNZST 43/3/2, 43/4/2, and 43/5/2 can be stabilized into a commensurate antiferroelectric phase at low temperatures. For PNZST 43/4/2, this occurs at −30 °C during cooling. The incommensurate antiferroelectric phase in this ceramic exists between −30 and 144 °C, the multicell cubic phase is stable between 144 and 195 °C, while the paraelectric phase exists above 195 °C. The Raman spectra that are characteristic to these phases were recorded during cooling at different temperatures and are shown in figure 10. At 250 °C, the paraelectric cubic phase has the space group $Pm3m$, there is no Raman active mode. As a consequence, no peaks between 40 and 360 cm^{-1} were detected in the spectrum. When cooled down to 165 °C, a multicell cubic state is expected. However, there are still no strong Raman modes detected in the spectrum. At 25 °C, the antiferroelectric phase with incommensurate modulations shows the mode A, as indicated in figure 10. Further

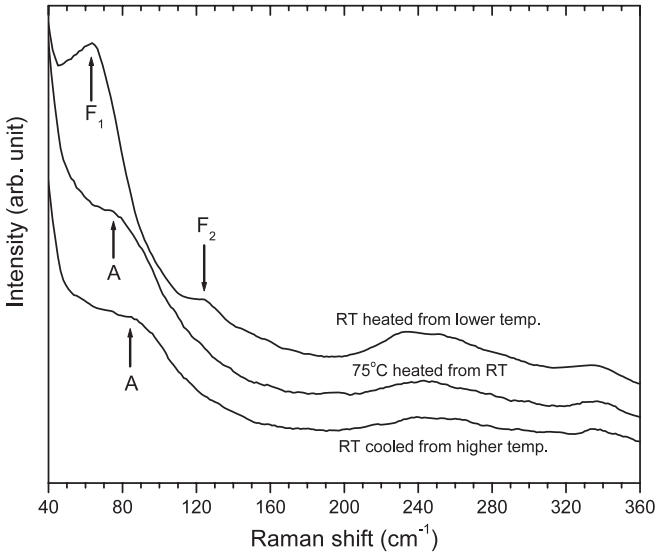

Figure 9. Thermal history effect in PNZST 43/8/2 revealed by Raman spectroscopy.

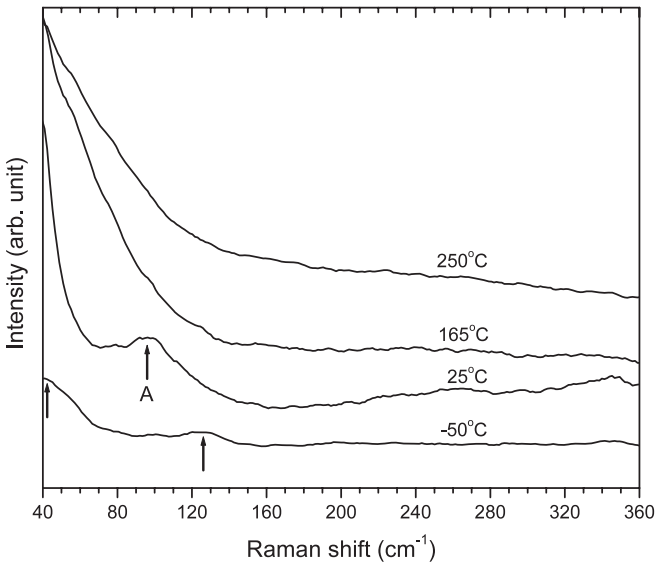

Figure 10. The commensurate antiferroelectric, the incommensurate antiferroelectric, the multicell cubic and the paraelectric cubic phases in PNZST 43/4/2 revealed by Raman spectroscopy.

cooling to −50 °C develops the commensurate antiferroelectric phase and the Raman spectrum shows two strong modes, one around 40 cm^{-1} and the other at 129 cm^{-1} (marked by two arrows in figure 10). Presumably the commensurate antiferroelectric phase is isostructural to $PbZrO_3$ with the space group $Pbam$. And indeed, these two modes are consistent with previous Raman studies on $PbZrO_3$ [18]. Therefore, Raman spectroscopy is capable of discerning the two antiferroelectric phases, one with the commensurate the other with the incommensurate modulations.

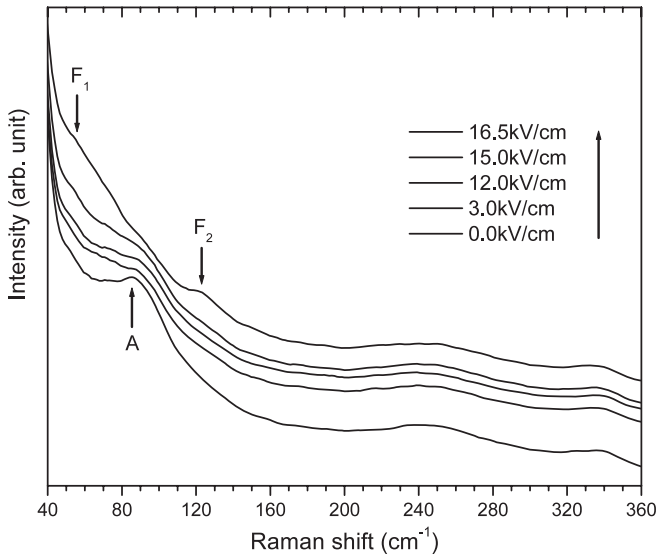

Figure 11. The electric field-induced antiferroelectric-to-ferroelectric phase transition in PNZST 43/7/2 revealed by Raman spectroscopy.

The phase diagram shown in figure 5 indicates that the electric field-induced antiferroelectric-to-ferroelectric phase transition occurs at 14 kV cm^{-1} in PNZST 43/7/2 at room temperature. This transition process was characterized with Raman spectroscopy with electric fields applied *in situ*. As shown in figure 11, a strong mode A is detected initially. At 3.0 kV cm^{-1}, mode A starts to soften. However, the softening process is slow and the mode can still be detected at the field of 15 kV cm^{-1}. When the field level increases to 16.5 kV cm^{-1}, mode A is dramatically weakened. At the same time, modes F_1 and F_2 emerge, indicating the development of the ferroelectric phase. The minor discrepancy in E_F determined by hysteresis loop measurement and Raman spectroscopy study may be resulted from a geometric effect. The Raman experiment detects only surface grains and the electric field was applied in plane, while the polarization measurement characterizes the bulk of the sample with electric field applied along the thickness direction.

As revealed by the hysteresis loop measurement shown in figure 4(b), the recovery of the antiferroelectric phase from the field-induced ferroelectric phase in the PNZST 43/7/2 ceramic is a slow process. This time-induced reverse phase transition process is examined with Raman spectroscopy. As shown in figure 12, strong peaks of modes F_1 and F_2 were observed right after the electric poling at 20 kV cm^{-1}. These two peaks decayed continuously with time. The mode A, signature of the antiferroelectric order, could be barely detected after 1 h. However, an obvious peak was observed for mode A after 4 h. At the same time, modes F_1 and F_2 softened significantly. After 150 h, a strong peak for mode A was developed. Residuals of peaks for the F_1 and F_2 modes can still be seen. Therefore, the time-induced reverse phase transition in PNZST 43/7/2 occurs on a timescale of hours.

4. Conclusions

Raman spectroscopy studies have been conducted to characterize the composition-, temperature-, electric field-, and time-induced phase transitions in $Pb_{0.99}Nb_{0.02}[(Zr_{0.57}Sn_{0.43})_{1-y}$

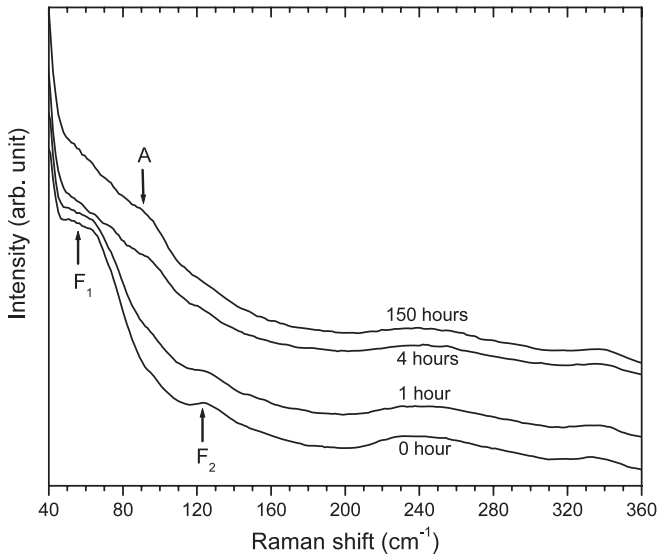

Figure 12. The time-induced reverse transition at room temperature from the metastable ferroelectric phase in PNZST 43/7/2.

$Ti_y]_{0.98}O_3$ ceramics. It is found that at room temperature, antiferroelectric order is developed in ceramics with $y = 0.03$–0.08, while ferroelectric order is developed in ceramics with $y = 0.10$ and 0.12. The incommensurate antiferroelectric phase in this composition series is characterized by the presence of a Raman mode around 90 cm^{-1}, and the ferroelectric phase displays strong modes around 60 and 125 cm^{-1}. Little difference is noticed between the paraelectric cubic phase and the multicell cubic phase in the Raman spectra, however, a different set of Raman modes is observed in the commensurate antiferroelectric phase from the incommensurate antiferroelectric phase. As revealed by Raman spectroscopy, the electric field-induced antiferroelectric-to-ferroelectric transition in PNZST 43/7/2 takes place gradually as field increases, and the reverse transition at zero field takes up to 4 h.

Acknowledgments

This work was supported by the Petroleum Research Fund through contract PRF# 42301-G5. The authors acknowledge access to the Raman Spectrometer in Professor Steve Martin's group at Iowa State University.

References

[1] Berlincourt D, Krueger H H A and Jaffe B 1964 *J. Phys. Chem. Solids* **25** 659
[2] Pan W Y, Dam C Q, Zhang Q M and Cross L E 1989 *J. Appl. Phys.* **66** 6014
[3] Xu B, Cross L E and Bernstein J J 2000 *Thin Solid Films* **377** 712
[4] Yang P and Payne D A 1992 *J. Appl. Phys.* **71** 1361
[5] Markowski K, Park S E, Yoshikawa S and Cross L E 1996 *J. Am. Ceram. Soc.* **79** 3297
[6] Viehland D, Forst D, Xu Z and Li J F 1995 *J. Am. Ceram. Soc.* **78** 2101
[7] Viehland D, Dai X H, Li J F and Xu Z 1998 *J. Appl. Phys.* **84** 458
[8] Chang Y, Lian J and Wang Y 1985 *Appl. Phys.* A **36** 221
[9] Speck J S, De Graef M, Wilkinson A P, Cheetham A K and Clarke D R 1993 *J. Appl. Phys.* **73** 7261

[10] Ricote J, Corker D L, Whatmore R W, Impey S A, Glazer A M, Dec J and Roleder K 1998 *J. Phys.: Condens. Matter* **10** 1767
[11] Knudsen J, Woodward D I and Reaney I 2003 *J. Mater. Res.* **18** 262
[12] He H and Tan X 2004 *Appl. Phys. Lett.* **85** 3187
[13] He H and Tan X 2005 *Phys. Rev.* B **72** 024102
[14] Burns G and Scott B A 1970 *Phys. Rev. Lett.* **25** 1191
[15] Bismayer U 1990 *Phase Transit.* **27** 211
[16] Meng J F, Katiyar R S, Zou G T and Wang X H 1997 *Phys. Status Solidi* a **164** 851
[17] Dobal P S and Katiyar R S 2002 *J. Raman Spectrosc.* **33** 405
[18] Pasto A E and Condrate R A Sr 1973 *J. Am. Ceram. Soc.* **56** 436
[19] Roleder K, Kugel G E, Fontana M D, Handerek J, Lahlou S and Carabatos-Nedelec C 1989 *J. Phys.: Condens. Matter* **1** 2257
[20] Hafid M, Handerek J, Kugel G E and Fontana M D 1992 *Ferroelectrics* **125** 477
[21] El-Harrad I, Becker P, Carabatos-Nedelec C, Handerek J, Juma Z and Dmytrow D 1995 *J. Appl. Phys.* **78** 5581
[22] Kojima S and Dong X 1998 *Japan. J. Appl. Phys.* **37** 5400
[23] Kojima S, Ohta N and Dong X 1999 *Japan. J. Appl. Phys.* **38** 5674
[24] Souza Filho A G, Freire P T C, Sasaki J M, Guedes I, Mendes Filho J, Melo F E A, Araujo E B and Eiras J A 1999 *Solid State Commun.* **112** 383
[25] Souza Filho A G, Freire P T C, Ayala A P, Sasaki J M, Guedes I, Mendes Filho J, Melo F E A, Araujo E B and Eiras J A 2000 *J. Phys.: Condens. Matter* **12** 7295
[26] Souza Filho A G, Faria J L B, Freire P T C, Ayala A P, Sasaki J M, Melo F E A, Mendes Filho J, Araujo E B and Eiras J A 2001 *J. Phys.: Condens. Matter* **13** 7305
[27] Tutuncu G, He H, Tan X and Ustundag E 2007 in preparation
[28] Viehland D, Forst D and Li J 1994 *J. Appl. Phys.* **75** 4137